Research Article Vol. 14, No. 8 / 1 Aug 2023 / Biomedical Optics Express 4237
Biomedical Optics EXPRESS

Volumetric live-cell autofluorescence imaging using Fourier light-field microscopy

ZHI LING,[1,2,3] KEYI HAN,[1] WENHAO LIU,[1] XUANWEN HUA,[1] AND SHU JIA[1,2,*]

[1]The Wallace H. Coulter Department of Biomedical Engineering, Georgia Institute of Technology and Emory University, Atlanta, GA 30332, USA
[2]Parker H. Petit Institute for Bioengineering and Biosciences, Georgia Institute of Technology, Atlanta, GA 30332, USA
[3]George W. Woodruff School of Mechanical Engineering, Georgia Institute of Technology, Atlanta, GA 30332, USA
[*]shu.jia@gatech.edu

Abstract: This study introduces a rapid, volumetric live-cell imaging technique for visualizing autofluorescent sub-cellular structures and their dynamics by employing high-resolution Fourier light-field microscopy. We demonstrated this method by capturing lysosomal autofluorescence in fibroblasts and HeLa cells. Additionally, we conducted multicolor imaging to simultaneously observe lysosomal autofluorescence and fluorescently-labeled organelles such as lysosomes and mitochondria. We further analyzed the data to quantify the interactions between lysosomes and mitochondria. This research lays the foundation for future exploration of native cellular states and functions in three-dimensional environments, effectively reducing photodamage and eliminating the necessity for exogenous labels.

1. Introduction

Imaging cell autofluorescence is crucial for understanding cellular structures and functions, as it allows researchers to visualize naturally occurring fluorescent molecules within cells without the need for exogenous labeling [1,2]. To date, various endogenous fluorophores, such as porphyrins, flavins, NAD(P)H, lipofuscin, and ceroid pigments, have been identified as responsible for cellular autofluorescence [3–5]. As a result, non-invasive probing of these autofluorescent signals minimizes potential perturbations to the native cellular state, gaining us more accurate observations and insights into the cellular metabolism, oxidative stress, and other translational implications [6–8].

In particular, fluorescence microscopy has been one of the major driving forces for investigating autofluorescence-relevant biological processes [1,9]. However, unlike exogenous fluorescent probes, the intensity and specificity of autofluorescence can be highly variable and heterogeneous, making the autofluorescent signals challenging to distinguish from the cellular space [10]. For instance, conventional epi-fluorescence systems have difficulty visualizing volumetric autofluorescent signals due to the lack of optical sectioning [11]. Confocal or two-photon laser-scanning microscopy offers improved sectioning and 3D ability, but the scanning process can be slow and may cause photodamage for capturing delicate autofluorescent signals [12]. In contrast, light-sheet microscopy provides effective optical sectioning without significant photobleaching and altered physiology of living cells [13,14], but the scanning mechanism may remain suboptimal for recording fast-moving molecules due to the inadequate volumetric time resolution.

Alternatively, the emergence of light-field microscopy (LFM) suggests a promising approach to fast, 3D imaging of autofluorescent molecules. LFM allows for the computational reconstruction of the volume of a biological specimen using a single camera frame [15]. Recent advancements

#495506 https://doi.org/10.1364/BOE.495506
Journal © 2023 Received 15 May 2023; revised 13 Jul 2023; accepted 14 Jul 2023; published 25 Jul 2023

Biomedical Optics EXPRESS

in Fourier LFM (FLFM, or XFLFM, i.e., extended LFM) have addressed the inherent uneven sampling of optical signals in traditional LFM, resulting in significantly improved volumetric image quality and computational efficiency [16–18]. Specifically, compared to conventional fluorescence microscopy, both the conventional and Fourier light-field strategies have been demonstrated particularly advantageous for live-cell imaging with subcellular, milliseconds spatiotemporal resolution [19–21].

Hence, the light-field approach holds great potential for rapid, single-shot, and scanning-free imaging of autofluorescence and associated dynamic cellular processes while minimizing photodamage per volumetric acquisition compared to other fluorescent microscopy methods. In this study, we advanced an FLFM-based approach for live-cell autofluorescence imaging. Specifically, we demonstrated lysosomal autofluorescence in fibroblasts and HeLa cells. Additionally, we conducted multicolor imaging and analysis to concurrently observe autofluorescent particles within lysosomes and their interactions with fluorescence-labeled organelles such as mitochondria. We expect this research to pave the path for future investigations of native cellular states and functions in 3D environments with minimum photodamage and invasiveness.

2. Methods

2.1. Experimental system and volumetric reconstruction

The system was constructed on the basis of our recently developed high-resolution Fourier light-field microscope (HR-FLFM) [19,21]. In brief, the setup utilizes an epi-fluorescence microscope (Nikon Eclipse Ti2-U) equipped with a 100×, 1.45 NA objective lens (Nikon CFI Plan Apochromat Lambda 100× Oil) and multicolor laser lines (561 and 488 nm, MPB) **(Fig. 1(a))**. Fluorescent emissions were collected using a quad-band dichroic mirror (ZT405/488/ 561/647, Chroma) and a corresponding emission filter (ZET405/488/561/647 m, Chroma). The native image plane (NIP) of the objective lens was Fourier transformed using a Fourier lens ($f_{\mathrm{FL}} = 275$ mm, Thorlabs). The microlens array (MLA, pitch $d = 3.25$ mm, f-number = 36, $f_{\mathrm{ML}} = 117$ mm, RPC Photonics) was placed on the conjugated pupil plane of the system, forming three elemental images by the corresponding microlenses on an sCMOS camera (ORCA-Flash 4.0, physical pixel size $P_{\mathrm{cam}} = 6.5$ µm, Hamamatsu).

Time-lapse sequences with an exposure time of 250 ms were collected to capture single-color images of the autofluorescent signals. For two-color imaging of lysosomal autofluorescence and fluorescently-labeled lysosomes or mitochondria, an acousto-optic tunable filter (AOTF) was controlled by a Python script to switch two laser lines on and off alternatively. Camera acquisition was synchronously triggered while the laser remained on. This permits FLFM to capture the dynamics and interactions of organelles from two channels **(Fig. 1(b))**. To process the images, raw light-field images were initially background-subtracted and processed with a lab-written ACsN denoising framework [22], an essential step for the successful reconstruction of relatively weak autofluorescent signals.

To reconstruct the 3D volume from a 2D light-field image, a wave-optics-based Richardson-Lucy algorithm was used through 20 deconvolution iterations between the elemental images and the 3D PSF of the system [23]. In principle, this method acquires the volume by iteratively conducting a forward projection ($HI_0^{(k)}$), which projects the 3D object onto the 2D camera plane, and a backward projection ($H^T I_C$), which takes the inverse process:

$$I_0^{(k+1)} = diag\{diag\{H^T H I_0^{(k)}\}^{-1}(H^T I_C)\} I_0^{(k)}$$

where $I_0^{(k)}$ represents the k^{th} calculated volume, I_C represents the camera image, and the measurement matrix H is determined by the PSF. A hybrid PSF method was implemented, which calibrated the position of numerically simulated PSF with the information of experimental PSF

Biomedical Optics EXPRESS

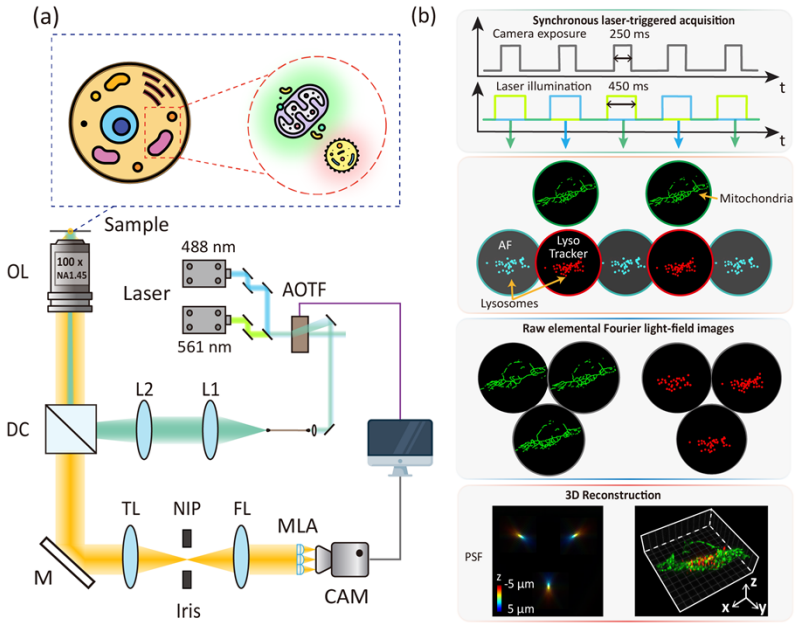

Fig. 1. Multicolor, high-resolution Fourier light-field microscopy for autofluorescence imaging. (a) Experimental setup for the two-color HR-FLFM system, implemented with 561-nm and 488-nm laser lines. The sample is acquired by an objective lens (OL) and a tube lens (TL), forming its image at the native image plane (NIP). The Fourier lens (FL) transforms the NIP to its back focal plane, where a microlens array (MLA) is placed. The MLA produces light-field elemental images recorded by an sCMOS camera. DC, dichroic cube; M, mirror; CAM, camera. (b) Laser illumination is controlled by an acousto-optic tunable filter (AOTF) using a Python script. Camera acquisition is synchronously triggered with laser illumination. A hybrid point-spread function (PSF) is collected from three elemental images within an axial depth range from -5 µm to 5 µm for the volumetric reconstruction of the light-field signals. AF, autofluorescence.

to enhance image quality [21]. The 3D reconstruction algorithm is available through our GitHub repository (https://github.com/ShuJiaLab/HR-FLFM).

2.2. Materials and sample preparation

The imaging experiments were performed with HeLa cells (#93021013, Sigma-Aldrich) and fibroblasts. Both cells were maintained at 37°C and in a 5% CO_2 atmosphere. The HeLa cells were cultured in Dulbecco's modified Eagle medium (DMEM, #10-013-CV, Corning) with 10% fetal bovine serum (FBS, #35-011-CV, Corning) and 1% Penicillin-Streptomycin (Pen-Strep, #15140-122, ThermoFisher). The culture medium for fibroblasts was made of DMEM (#11965-084, ThermoFisher) with supplements of 10% FBS (#35-011-CV, Corning), 1% GlutaMAX (#35050061-050, ThermoFisher), 1% MEM Non-Essential Amino Acids (MEM NEAA, #11140-050, ThermoFisher), 1% Antibiotic Antimycotic solution (#15240-096, ThermoFisher) and extra additive of 4 mg/mL AlbuMAX II (#11021029, Thermofisher).

For single-color autofluorescence imaging, the cells were removed from their medium and then washed using Hank's Balanced Salt Solution without phenol red (HBSS, #21-022-CVR, Corning) for two times before imaging in FluoroBrite DMEM (#A1896701, ThermoFisher). For multicolor imaging, the labeling of mitochondria was done by incubating the cell sample in a culture medium loaded with 100 nM MitoTracker Green FM (M7514, ThermoFisher) for

Biomedical Optics EXPRESS

20 min at 37 °C and 5% CO_2. After the incubation, the staining solution was removed, and the cells were thoroughly washed (2 times with HBSS) before being imaged in FluoroBrite DMEM (#A1896701, ThermoFisher) with additional 10 mM glucose (G7528-250 G, Sigma). For fluorescent labeling of lysosomes, cells were incubated in a culture medium loaded with 50 mM LysoTracker Green FM (L7526, ThermoFisher) for 30 min at 37 °C and 5% CO_2. The washing and imaging protocols were the same as above.

3. Results

3.1. Imaging lysosomal autofluorescence in living HeLa cells and fibroblasts

Lipofuscin and lipofuscin-like pigments are endogenous biomolecules exhibiting a fluorophore-like activity [4]. As the aggregation of undigested cell materials, lipofuscin is accumulated within lysosomes, preferentially within postmitotic cells such as neurons, cardiomyocytes, and other senescent cells [24,25]. In this work, we first imaged the autofluorescence generated from lipofuscin in living HeLa cells and fibroblasts. In particular, under the 561-nm excitation [26,27], autofluorescent signals were clearly observed in the cytoplasm (**Fig. 2(a)**), and the reconstructed 3D volume displayed discrete subcellular granular structures across a depth range > 4 μm (**Fig. 2(b,c)**). Notably, the ACsN restoration facilitated the viable recovery of the volumetric details, which were otherwise restricted by the low signal-to-noise ratio of the autofluorescent images. The single-shot, volumetric property of the light-field approach allows for minimum volumetric photodamage on the cells, enabling continuous observation and 3D tracking of the dynamic processes of the lipofuscin granules over tens of seconds without noticeable photobleaching (**Fig. 2(d,e)**). Furthermore, the reconstructed autofluorescent images exhibited full width at half maximum (FWHM) values of ~400 nm and ~700 nm in the lateral and axial dimensions, respectively (**Fig. 2(f)**), consistent with the convolution of the known lipofuscin size (~0.5 μm [28]) with the 3D resolution (400-600 nm) of the HR-FLFM system [21].

3.2. Imaging lysosomal autofluorescence and labeled lysosomes in living fibroblasts

Next, to verify the lysosomal origin of the observed autofluorescence, as reported in previous studies [4,25], we stained fibroblasts with Lyso-Tracker and excited them with 488 nm and 561 nm lasers. We ensured no interference between the two channels by employing a custom-written Python script that regulated the AOTF and, thus, the sequential laser illumination (**Fig. 1(b)**). We set the camera exposure time to 250 ms, with each laser channel receiving an illumination time of 450 ms, followed by a 200-ms interval to allow for minimum but sufficient transfer time from the computer to the hardware. Our results demonstrated that lipofuscin granules were predominantly co-located within lysosomes, as observed from their reconstructed 3D images (**Fig. 3(a)**). Notably, the system was capable of capturing the concurrent motion of labeled and intrinsic signals, exhibiting a strong correlation between lysosomes and lipofuscin granules in the x ($r = 0.96$, $p < 0.01$), y ($r = 0.90$, $p < 0.01$) and z ($r = 0.90$, $p < 0.01$) dimensions (**Fig. 3(b-e)**). As an essential characteristic desirable for autofluorescent imaging, the single-shot property of the system allows for the continuous observation of the autofluorescent lipofuscin for more than tens of seconds with minimal photodamage, capturing the lipofuscin particles moving at an average speed of 0.38 μm/s (**Fig. 3(f)**). With the ability to accurately visualize and track lipofuscin granules within lysosomes in living cells, this research enables a better investigation of the dynamics of lipofuscin and its association with lysosomal function.

3.3. Imaging mitochondria and lysosomal autofluorescence in living HeLa cells

The intricate interplay between mitochondrial and lysosomal functions is essential for maintaining cellular homeostasis, and the dysregulation of both organelles has been implicated in numerous diseases [29,30]. Recently, research on the lysosomal enzyme trafficking pathway

Biomedical Optics EXPRESS

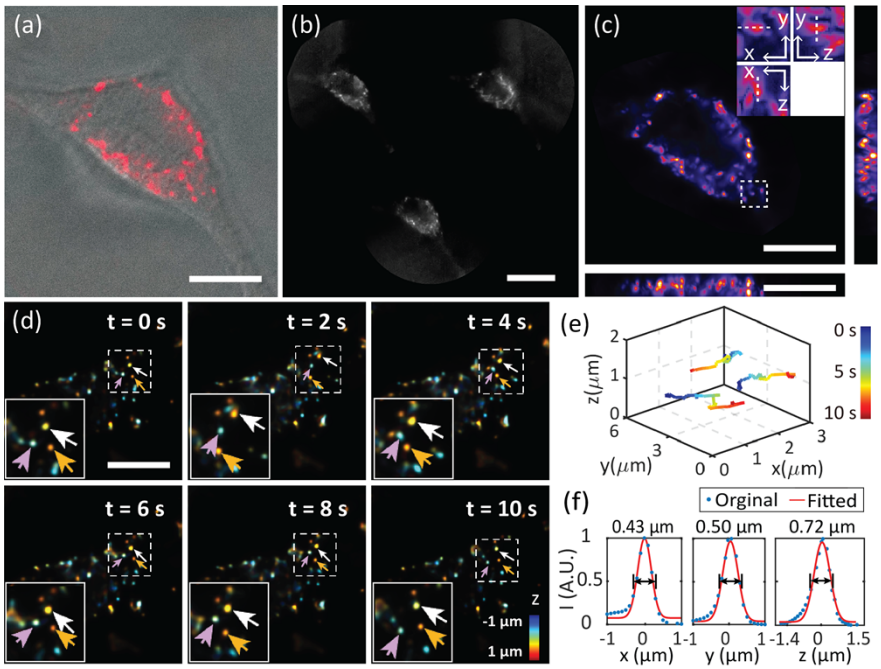

Fig. 2. Imaging lipofuscin autofluorescence in living cells using HR-FLFM. (a) Overlay of bright-field and epi-autofluorescent images of lipofuscin granules in living HeLa cells. (b,c) Corresponding raw light-field image (b) and 3D max intensity projection (MIP) of reconstructed volume (c). (d) Depth-color-coded stack projection across a 2-µm range of the 3D volume reconstructed from a time-lapsed light-field sequence of lipofuscin autofluorescence in fibroblasts taken at a volume acquisition time of 250 ms. Insets display the movement of the arrow-indicated granules in the dashed-boxed regions. (e) 3D tracking of three exemplary lipofuscin granules marked by the arrows in (d) at the nanometer scale over a 10-s course (time-color-coded). (f) Cross-sectional profiles of the autofluorescent molecule along the dashed lines in the boxed region in (c), exhibiting FWHM values of 0.43 µm, 0.50 µm, and 0.72 µm in x, y, and z, respectively. Scale bars: 10 µm (a-d).

and mitochondria-lysosome communication has gained considerable attention, underscoring the pivotal role of lysosomes as a cellular nexus contributing to human health [31,32]. To facilitate future insights into the inter-organelle interactions, we performed time-lapse experiments utilizing dual-color HR-FLFM, in which fluorescently-labeled mitochondria and autofluorescent lipofuscin particles were excited with the 488-nm and 561-nm lasers, respectively (**Fig. 4(a,b)**). The reconstructed two-color images revealed the structural relationship of lipofuscin particles with mitochondrial spheroids (**Fig. 4(c)**).

We then developed an algorithm to analyze the image results. Specifically, first, mitochondrial positions were ascertained through thresholding and skeletonizing on the 3D reconstructed image stacks (**Fig. 4(d)**). Next, the central positions of all lipofuscin particles in the corresponding image stacks were determined and tracked over time (**Fig. 4(e)**) using a Fiji-plugin function (i.e., 3D Maxima Finder [33]). Then, the 3D distances between the center of each lipofuscin particle and the mitochondrial skeletons were then calculated based on the nearest neighbor search (**Fig. 4(f)**) [34]. Notably, the nearest neighbors in the 3D space of the lipofuscin particles on the mitochondrial skeletons differ from the results determined by 2D image projections, indicating a more precise measurement with the 3D method (**Fig. 4(f, inset)**).

Biomedical Optics EXPRESS

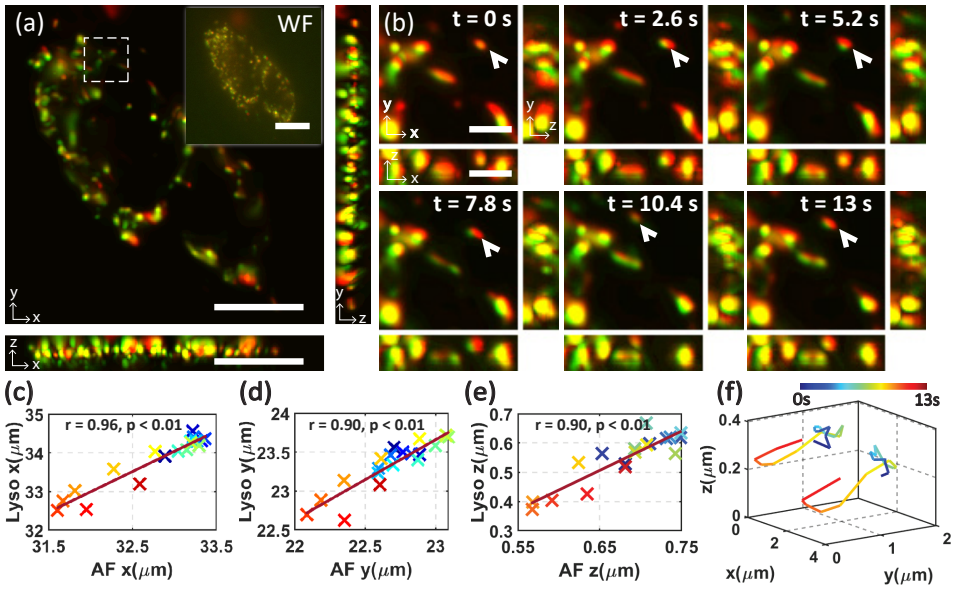

Fig. 3. Imaging lipofuscin autofluorescence and fluorescently-labeled lysosomes in living fibroblasts. (a) Two-color MIP of the 3D reconstructed volume of a fibroblast at t = 0 s. The green color represents fluorescence from lysotracker-labeled lysosomes, while the red represents lipofuscin autofluorescence. Inset shows the corresponding 2D wide-field image. (b) Zoomed-in 3D images of the boxed region in (a) at t = 0 s, 2.6 s, 5.2 s, 7.8 s, 10.4 s, 13 s. (c,d) Linear fitting of the x-coordinates (c), y-coordinates (d), and z-coordinates (e) of the autofluorescent particle and the corresponding lysosome as marked by the white arrows in (b). (f) 3D tracking of the autofluorescent particle and the corresponding lysosome as marked by the white arrows in (b) over 13 s, exhibiting concurrent trajectories. The time points are color-coded according to the color bar. Scale bars: 10 μm (a), 2.5 μm (b).

The spatiotemporal resolution and volumetric ability of HR-FLFM allow for the continuous acquisition of the positions of each lipofuscin granule in the 3D cellular space. By localizing their positions relative to the mitochondria, distance variations between the two can be recorded and visualized over time (**Fig. 4(g)**). The resulting distribution of inter-organelle distances, for instance, was obtained from a HeLa cell containing 68 clusters of lipofuscin particles at $t = 0$ s (**Fig. 4(h)**). The distance distribution peaked at 0.66 μm, and 97% of the lipofuscin particles were located within a 2-μm distance, corroborating prior studies that measured distances between endo-lysosomes and mitochondria [35].

Furthermore, contact events between mitochondria and autofluorescent molecules can be visualized by a heatmap exhibiting the temporal changes in distance from 68 identified lipofuscin particles to their nearest mitochondrial neighbors (**Fig. 4(i)**). In particular, the system allowed for observing the events in detail from the 3D rendering of a magnified area segmented from the reconstructed series of volumes (**Fig. 4(j)**). Our method offers the 3D volumetric identification of autofluorescent lipofuscin particles as effective biomarkers for lysosomal and mitochondrial activities [27,36]. Future research may combine dynamic imaging with super-resolution techniques to determine mitochondria-lysosome contacts at various functional endpoints, ultimately offering valuable insights into the distribution and dynamic crosstalk between these two crucial organelles [37,38].

Biomedical Optics EXPRESS

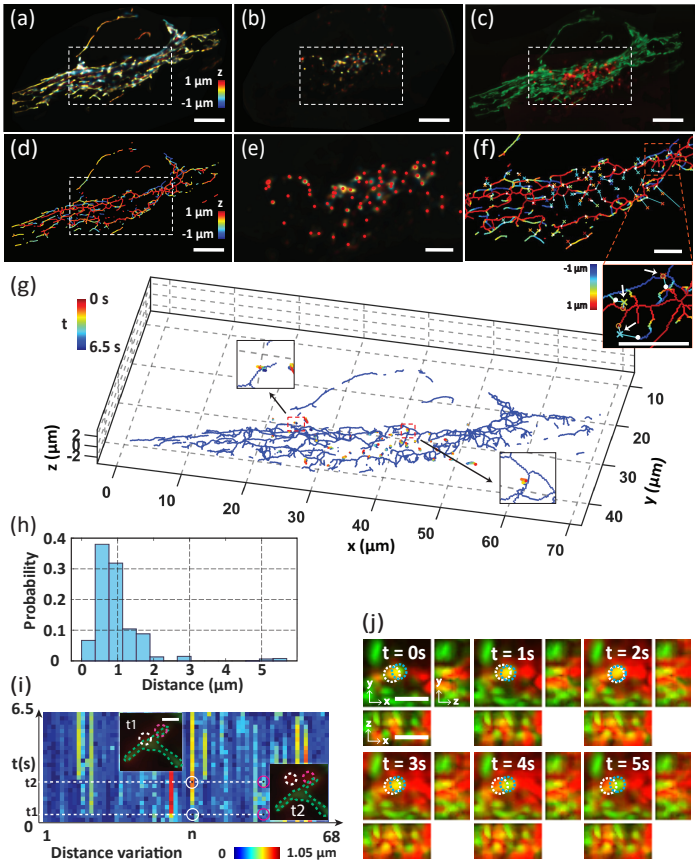

Fig. 4. Imaging lipofuscin autofluorescence and fluorescently-labeled mitochondria in living HeLa cells. (a,b) Color-coded stack projection across a 2-μm depth range of the 3D reconstructed volume of fluorescently-labeled mitochondria (a) and lipofuscin autofluorescent particles (b) in HeLa cells at t = 0 s. (c) Merged two-color MIP image of the reconstructed mitochondria (green) and lipofuscin particles (red) at t = 0 s. (d,e) Color-coded skeletonized mitochondrial image stack projection (d) and the 3D central position of each lipofuscin particle, as marked by red dots in (e), are used to calculate the distance between the lipofuscin particles and mitochondria. (f) Zoomed-in image of the boxed region in (d), with the 3D position of each lysosome (depth-color-coded, marked 'x') mapped onto the mitochondrial skeleton. The nearest point on the neighboring mitochondria of a lysosome is marked in white dots, and connecting lines from the point to the lysosome are marked in cyan. Inset shows the zoomed-in image of the boxed region, with the white arrows pointing to lipofuscin particles and white dots indicating their nearest neighbors on mitochondria in the 3D space, compared to the less precise nearest neighbors derived based on 2D analysis. (g) Visualization of the lipofuscin particle movement with respect to the mitochondria over the time course. Trajectories of the lipofuscin particles at each frame were color-coded according to the color scale bar. (h) Distribution of the 3D distance between the 68 segmented lipofuscin particles and mitochondria. (i) Heatmap of the distance variation between lipofuscin particles and mitochondria for every particle (n) over the time course (t). Each pixel on the heatmap indicates the distance based on the color bar. (j) Two-color MIP of the 3D reconstructed volumes from the time-lapse recording of mitochondria (green) and lipofuscin (red). An example contact event is illustrated with mitochondria and lipofuscin marked with blue and white circles, respectively, displaying the distance variation over 5 s. Scale bars: 10 μm (a-d), 20 μm (e,f), 2 μm (j), 1 μm (i).

Biomedical Optics EXPRESS

4. Conclusion

We have demonstrated high-resolution light-field imaging for studying intrinsic autofluorescent signals of living cells. This system enables scanning-free, single-shot, and sensitive recording of moving autofluorescent molecules in the 3D cellular space. Our method was employed to observe lysosomal autofluorescence, offering an additional channel for monitoring inter-organelle communication in both stained and unstained cells. The approach provides a quantification protocol to facilitate future investigations into the intricate interactions between multiple organelles [31]. This platform, based on an epi-fluorescence microscope, can be integrated with other imaging modalities, such as light-sheet microscopy, to enhance image quality and isotropic resolution [39,40], various live-cell imaging protocols [41], and imaging flow cytometry and machine learning [42], to further enhance the applicability, 3D image throughput, and analysis. We anticipate the approach to minimize perturbation to living cells and foster a comprehensive understanding of cellular physiology, functions, and diseases.

Funding. National Science Foundation (DBI2145235, EFMA1830941); National Institutes of Health (R35GM124846).

Disclosures. The authors declare that there are no conflicts of interest to this article.

Data availability. Data underlying the results presented in this paper are not publicly available at this time but may be obtained from the authors upon reasonable request.

References

1. A. C. Croce and G. Bottiroli, "Autofluorescence spectroscopy and imaging: a tool for biomedical research and diagnosis," Eur. J. Histochem. **58**(4), 2461 (2014).
2. M. Monici, "Cell and tissue autofluorescence research and diagnostic applications," Biotechnol. Annu Rev. **11**, 227–256 (2005).
3. H. Schneckenburger, M. Lang, T. Köllner, A. Rück, M. Herzog, H. Hörauf, and R. Steiner, "Fluorescence spectra and microscopic imaging of porphyrins in single cells and tissues," Lasers Med. Sci. **4**(3), 159–166 (1989).
4. G. Di Guardo, "Lipofuscin, lipofuscin-like pigments and autofluorescence," Eur. J. Histochem. **59**(1), 2485 (2015).
5. R. C. Benson, R. A. Meyer, M. E. Zaruba, and G. M. McKhann, "Cellular autofluorescence–is it due to flavins?" J. Histochem. Cytochem. **27**(1), 44–48 (1979).
6. I. Miranda-Lorenzo, J. Dorado, E. Lonardo, S. Alcala, A. G. Serrano, J. Clausell-Tormos, M. Cioffi, D. Megias, S. Zagorac, A. Balic, M. Hidalgo, M. Erkan, J. Kleeff, A. Scarpa, B. Sainz Jr., and C. Heeschen, "Intracellular autofluorescence: a biomarker for epithelial cancer stem cells," Nat. Methods **11**(11), 1161–1169 (2014).
7. Y. F. Qin and Y. Q. Xia, "Simultaneous Two-Photon Fluorescence Microscopy of NADH and FAD Using Pixel-to-Pixel Wavelength-Switching," Front. Phys. **9**, 642302 (2021).
8. O. I. Kolenc and K. P. Quinn, "Evaluating Cell Metabolism Through Autofluorescence Imaging of NAD(P)H and FAD," Antioxid Redox Sign **30**(6), 875–889 (2019).
9. J. I. Garcia-Plazaola, B. Fernandez-Marin, S. O. Duke, A. Hernandez, F. Lopez-Arbeloa, and J. M. Becerril, "Autofluorescence: Biological functions and technical applications," Plant Sci. **236**, 136–145 (2015).
10. M. E. Gosnell, A. G. Anwer, S. B. Mahbub, S. Menon Perinchery, D. W. Inglis, P. P. Adhikary, J. A. Jazayeri, M. A. Cahill, S. Saad, C. A. Pollock, M. L. Sutton-McDowall, J. G. Thompson, and E. M. Goldys, "Quantitative non-invasive cell characterisation and discrimination based on multispectral autofluorescence features," Sci. Rep. **6**(1), 23453 (2016).
11. S. V. E. Liu, A. Dhaliwal, M. D. Treiser, H.-J. Sung, and P. V. Moghe, "High Resolution Fluorescence Imaging of Cell–Biomaterial Interactions," Comprehensive Biomaterials II **3**, 406–423 (2017).
12. E. G. Reynaud, U. Kržič, K. Greger, and E. H. K. Stelzer, "Light sheet-based fluorescence microscopy: more dimensions, more photo ns, and less photodamage," HFSP J. **2**(5), 266–275 (2008).
13. E. H. K. Stelzer, F. Strobl, B. J. Chang, F. Preusser, S. Preibisch, K. McDole, and R. Fiolka, "Light sheet fluorescence microscopy," Nat. Rev. Methods Primers **1**(1), 73 (2021).
14. K. Samimi, D. Desa, W. Lin, K. Weiss, J. Li, J. Huisken, J. Chacko, A. Velten, J. Rogers, K. Eliceiri, and M. Skala, "Light-sheet autofluorescence lifetime imaging microscopy using a SPAD array detector (Conference Presentation)," in *SPIE BiOS* (SPIE, 2023).
15. M. Levoy, R. Ng, A. Adams, M. Footer, and M. Horowitz, "Light field microscopy," in *ACM SIGGRAPH 2006 Papers* (2006), pp. 924–934.
16. C. Guo, W. Liu, X. Hua, H. Li, and S. Jia, "Fourier light-field microscopy," Opt. Express **27**(18), 25573–25594 (2019).
17. L. Cong, Z. Wang, Y. Chai, W. Hang, C. Shang, W. Yang, L. Bai, J. Du, K. Wang, and Q. Wen, "Rapid whole brain imaging of neural activity in freely behaving larval zebrafish (Danio rerio)," Elife **6**, e28158 (2017).
18. W. Liu, G.-A. R. Kim, S. Takayama, and S. Jia, "Fourier light-field imaging of human organoids with a hybrid point-spr ead function," Biosens. Bioelectron. **208**, 114201 (2022).

Biomedical Optics EXPRESS

19. K. Han, X. Hua, V. Vasani, G.-A. R. Kim, W. Liu, S. Takayama, and S. Jia, "3D super-resolution live-cell imaging with radial symmetry and Fourier light-field microscopy," Biomed. Opt. Express **13**(11), 5574–5584 (2022).
20. Z. Lu, Y. Liu, M. Jin, X. Luo, H. Yue, Z. Wang, S. Zuo, Y. Zeng, J. Fan, Y. Pang, J. Wu, J. Yang, and Q. Dai, "Virtual-scanning light-field microscopy for robust snapshot high-resolution volumetric imaging," Nat. Methods **20**(5), 735–746 (2023).
21. X. Hua, W. Liu, and S. Jia, "High-resolution Fourier light-field microscopy for volumetric multi-color live-cell imaging," Optica **8**(5), 614–620 (2021).
22. B. Mandracchia, X. Hua, C. Guo, J. Son, T. Urner, and S. Jia, "Fast and accurate sCMOS noise correction for fluorescence microscopy," Nat. Commun. **11**(1), 94 (2020).
23. F. Dell'Acqua, G. Rizzo, P. Scifo, R. A. Clarke, G. Scotti, and F. Fazio, "A model-based deconvolution approach to solve fiber crossing in diffus ion-weighted MR imaging," IEEE Trans. Biomed. Eng. **54**(3), 462–472 (2007).
24. T.-R. Riew, H. L. Kim, J.-H. Choi, X. Jin, Y.-J. Shin, and M.-Y. Lee, "Progressive accumulation of autofluorescent granules in macrophages in rat striatum after systemic 3-nitropropionic acid: a correlative ligh t-and electron-microscopic study," Histochem. Cell Biol. **148**(5), 517–528 (2017).
25. D. A. Gray and J. Woulfe, "Lipofuscin and aging: a matter of toxic waste," Sci. Aging Knowl. Environ. **2005**(5), re1 (2005).
26. H. Zhang, C. Tan, X. Shi, and J. Xu, "Impacts of autofluorescence on fluorescence based techniques to study microglia," BMC Neurosci. **23**(1), 21 (2022).
27. A. Moreno-Garcia, A. Kun, O. Calero, M. Medina, and M. Calero, "An Overview of the Role of Lipofuscin in Age-Related Neurodegeneration," Front. Neurosci. **12**, 464 (2018).
28. C. L. Dolman and P. M. MacLeod, "Lipofuscin and its Relation to Aging," in *Advances in Cellular Neurobiology*, S. Fedoroff and L. Hertz, eds. (Elsevier, 1981), pp. 205–247.
29. Y. C. Wong, S. Kim, W. Peng, and D. Krainc, "Regulation and function of mitochondria–lysosome membrane contact site s in cellular homeostasis," Trends Cell Biol. **29**(6), 500–513 (2019).
30. W. Peng, Y. C. Wong, and D. Krainc, "Mitochondria-lysosome contacts regulate mitochondrial Ca2 + dynamics vi a lysosomal TRPML1," Proc. Natl. Acad. Sci. **117**(32), 19266–19275 (2020).
31. C. M. Deus, K. F. Yambire, P. J. Oliveira, and N. Raimundo, "Mitochondria-Lysosome Crosstalk: From Physiology to Neurodegeneration," Trends Mol. Med. **26**(1), 71–88 (2020).
32. C. Pechincha, S. Groessl, R. Kalis, M. de Almeida, A. Zanotti, M. Wittmann, M. Schneider, R. P. de Campos, S. Rieser, M. Brandstetter, A. Schleiffer, K. Muller-Decker, D. Helm, S. Jabs, D. Haselbach, M. K. Lemberg, J. Zuber, and W. Palm, "Lysosomal enzyme trafficking factor LYSET enables nutritional usage of extracellular proteins," Science **378**(6615), eabn5637 (2022).
33. J. Ollion, J. Cochennec, F. Loll, C. Escudé, and T. Boudier, "TANGO: a generic tool for high-throughput 3D image analysis for studying nuclear organization," Bioinformatics **29**(14), 1840–1841 (2013).
34. Z. Song and N. Roussopoulos, *K-nearest Neighbor Search for Moving Query Point*, (Springer, 2011), pp. 79–96.
35. A. D. Juhl, C. W. Heegaard, S. Werner, G. Schneider, K. Krishnan, D. F. Covey, and D. Wüstner, "Quantitative imaging of membrane contact sites for sterol transfer bet ween endo-lysosomes and mitochondria in living cells," Sci. Rep. **11**(1), 8927 (2021).
36. J. Konig, C. Ott, M. Hugo, T. Jung, A. L. Bulteau, T. Grune, and A. Hohn, "Mitochondrial contribution to lipofuscin formation," Redox Biol. **11**, 673–681 (2017).
37. Y. C. Wong, D. Ysselstein, and D. Krainc, "Mitochondria-lysosome contacts regulate mitochondrial fission via RAB7 GTP hydrolysis," Nature **554**(7692), 382–386 (2018).
38. K. Qiu, W. Zou, H. Fang, M. Hao, K. Mehta, Z. Tian, J.-L. Guan, K. Zhang, T. Huang, and J. Diao, "Light-activated mitochondrial fission through optogenetic control of m itochondria-lysosome contacts," Nat. Commun. **13**(1), 4303 (2022).
39. K. Samimi, D. E. Desa, W. Lin, K. Weiss, J. Li, J. Huisken, V. Miskolci, A. Huttenlocher, J. V. Chacko, A. Velten, J. D. Rogers, K. W. Eliceiri, and M. C. Skala, "Light-sheet autofluorescence lifetime imaging with a single-photon avalanche diode array," J. Biomed. Opt. **28**(06), 066502 (2023).
40. N. Wagner, N. Norlin, J. Gierten, G. de Medeiros, B. Balazs, J. Wittbrodt, L. Hufnagel, and R. Prevedel, "Instantaneous isotropic volumetric imaging of fast biological processes," Nat. Methods **16**(6), 497–500 (2019).
41. P. P. Laissue, R. A. Alghamdi, P. Tomancak, E. G. Reynaud, and H. Shroff, "Assessing phototoxicity in live fluorescence imaging," Nat. Methods **14**(7), 657–661 (2017).
42. D. M. D. Siu, K. C. M. Lee, B. M. F. Chung, J. S. J. Wong, G. Zheng, and K. K. Tsia, "Optofluidic imaging meets deep learning: from merging to emerging," Lab Chip **23**(5), 1011–1033 (2023).